2014

Tropical cyclone footprint in the ocean mixed layer observed by Argo in the Northwest Pacific

Fu, HongLi

AGU PUBLICATIONS

JGR

Journal of Geophysical Research: Oceans

RESEARCH ARTICLE

10.1002/2014JC010316

Tropical cyclone footprint in the ocean mixed layer observed by Argo in the Northwest Pacific

HongLi Fu[1], Xidong Wang[1], Peter C. Chu[2], Xuefeng Zhang[1], Guijun Han[1], and Wei Li[1]

[1]Key Laboratory of Marine Environmental Information Technology, SOA, National Marine Data and Information Service, Tianjin, People's Republic of China, [2]Naval Ocean Analysis and Prediction Laboratory, Department of Oceanography, Naval Postgraduate School, Monterey, California, USA

Key Points:
- Response of OML to different type of TCs is investigated using Argo profiles
- Rainfalls by the strong and slow TCs can increase barrier layer thickness
- Mixed layer deepening in summer is observed up to 5 m

Correspondence to:
X. Wang,
xidong_wang@yahoo.com

Citation:
Fu, H.L., X. Wang, P. C. Chu, X. Zhang, G. Han, and W. Li (2014), Tropical cyclone footprint in the ocean mixed layer observed by Argo in the Northwest Pacific, *J. Geophys. Res. Oceans*, *119*, 8078–8092, doi:10.1002/2014JC010316.

Received 15 JUL 2014
Accepted 20 OCT 2014
Accepted article online 25 OCT 2014
Published online 27 NOV 2014

Abstract This study systematically investigated the ocean mixed layer responses to tropical cyclone (TC) using available Argo profiles during the period of 1998–2011 in the northwest Pacific. Results reveal that isothermal layer (IL) deepening and isothermal layer (IL) cooling with evident rightward biases induced by strong TCs are clearer compared to the weak TCs. Likewise, the rightward biases of IL deepening and cooling induced by fast TCs are more obvious than that induced by slow TCs. The upwelling within TC's eye is much stronger for the strong (slow) TCs than weak (fast) TCs. For the strong and slow TCs, the TC-induced rainfall reduces deepening of constant density layer (with its depth called the mixed layer depth, MLD), and in turn increases the barrier layer thickness (BLT). The initial BL prior to TC can restrict IL cooling more markedly under the weak and fast TCs than under the strong and slow TCs. The inertial oscillation is stronger induced by the strong (fast) TCs than by the weak (slow) TCs. In addition, the most pronounced TC-induced mixed layer deepening and IL cooling in July to October climatology occur in the subtropical gyre of the northwest Pacific with enhanced vertical diffusivity. The maximum increase of isothermal layer depth (ILD) and MLD is up to 5 m, with IL cooling up to 0.4°C.

1. Introduction

Oceanic response to tropical cyclones (TCs) has been a hot topic due to its importance for climate change, ecological variability, and environmental protection. Many studies show that strong winds associated with TCs induce a decrease in isothermal layer temperature (ILT) and a deepening of isothermal layer (IL) beneath storms by vertical entrainment process due to turbulent mixing. The cooling and deepening are generally more evident on the right side of TC's tracks in the Northern Hemisphere [*Price*, 1981; *Shay et al*., 1992; *Chu et al*., 1999, 2000a; *Jacob et al*., 2000; *Zheng et al*., 2008; *Nam et al*., 2011]. Under storms, energy transferred from atmosphere to ocean generates upwelling, near-inertial waves, and currents [*Price et al*., 1994; *Wang and Huang*, 2004; *Liu et al*., 2008; *Jaimes and Shay*, 2010; *Chang et al*., 2012, 2013]. As TC's translation speed is less than phase speed of the first baroclinic mode, oceanic response tends to be barotropic, geostrophic, and cyclonic gyre with upwelling in the storm's center [*Chang and Anthes*, 1978; *Chang*, 1985; *Ginis and Sutyrin*, 1995], which weakens the IL deepening near the storm's centers [*Wu and Chen*, 2012]. If the TC's translation speed is faster than the phase speed of the first baroclinic mode, the currents in the wake become more near-inertial after the first half inertial period. The upper ocean changes, in turn, affect the change of typhoon intensity through the air-sea feedback mechanism [*Emanuel*, 1991]. The persistence of sea surface cooling for 1–2 months after the TC passage could potentially affect large-scale atmospheric circulation [*Hart et al*., 2007]. Several studies, based on observations and modeling, suggest that TC-induced energy input and mixing may play an important role in climate variability through regulating the oceanic general circulation and its variability [e.g., *Emanuel*, 2001; *Sriver and Huber*, 2007; *Liu et al*., 2008; *Hu and Meehl*, 2009; *Wang et al*., 2009; *Fedorov et al*., 2010; *Wang et al*., 2014].

To understand the interaction between ocean and TC, subsurface measurements following TC are important. The Array for Real-time Geostrophic Oceanography (Argo) floats measure the global ocean (0–2000 m) temperature and salinity even under extreme atmospheric and oceanic conditions such as TC passage, and thus provide a complete picture of the upper ocean structure and variability in response to TCs [*Roemmich and Owens*, 2000]. Statistical characteristics of mixed layer responses to typhoons in the North Pacific are obtained and examined by *Park et al*. [2005] using the Argo profiling float data from 2000 to 2003. The

results indicate that the changes in ILT and isothermal layer depth (ILD) are inversely correlated, and maximum cooling and deepening appear at midlatitude of 20°N–30°N, which is mainly associated with strong wind, slow translation speed of typhoons, and shallow background ILD. The linear regression (data from 2000 to 2005) between the Argo profile and wind speed [*Liu et al*., 2007] shows a weakly positive correlation between the ILD change and the wind speed, and implies that the high wind speeds not only induce strong vertical mixing (increasing ILD) but also cause upwelling (decreasing ILD). The response of the upper ocean to typhoons is reexamined in the northwest Pacific Ocean using the Argo profile data (2000–2008) with the seasonal variability removed [*Wu and Chen*, 2012]. The result reveals a delayed response of ILT relative to ILD and the longer restoring time of ILT. Above statistical analyses mainly reveal the local relationship (one-dimensional in vertical) between ILD and ILT from all TCs.

Although the two-dimensional response to TCs in the upper ocean has been studied [e.g., *Jacob et al*., 2000; *Chu et al*., 2000a], statistical verifications have yet been conducted using the longer period Argo profile data. Since the feedback of the upper ocean to TC mainly occurs during its passages, it is necessary to study the spatial structure of the instantaneous response of the upper ocean.

In regions of high freshwater input (i.e., heavy rainfall) where significant salinity stratification sets within a deep isothermal layer, a barrier layer can appear between the base of the isothermal layer and the base of the mixed layer (i.e., constant density layer, shallower than the isothermal layer) to change the thermohaline front [*Chu and Wang*, 2003], and to reduce the entrainment of the cool thermocline water into the isothermal layer [e.g., *Chu et al*., 2002; *Chu and Fan*, 2010, 2011; *Liu et al*., 2009]. Usually, the TC-induced sea surface cooling negatively feedbacks to TC intensification [e.g., *Schade and Emanuel*, 1999; *Cione and Uhlhorn*, 2003]. The reduction of entrainment weakens the TC-induced surface cooling [e.g., *Wang et al*., 2011; *Balaguru et al*., 2012], which in turn decreases the negative feedback effect of upper ocean to TC. However, due to the observational limitation, the BL variability during TC has yet been explored systematically.

With increasing number of Argo profiling floats deployed in the world's oceans over the past two decades, more detailed analysis on the oceanic response including BL to TCs can be conducted. In this study, all TCs during 1998–2011 are classified into four types according to their maximum sustained wind speeds (weak, strong) and translation speeds (slow, fast). The spatial and temporal variability of the instantaneous isothermal/mixed layer responses to the four types of TCs are analyzed and discussed, with the emphasis of the barrier layer variability during TC passage. Besides, the effect of TC on the isothermal/mixed layer climatology is also investigated based on the Argo observation of 1998–2011. The rest of the paper is organized as follows. Data source and processing are described in section 2. Section 3 presents the TC classification by maximum sustained wind speed or translation speed. Section 4 depicts the instantaneous isothermal/mixed layer responses to four types of TCs. Section 5 discusses the temporal-spatial variability of the isothermal/mixed layer responses to the four TC types. Section 6 investigates the effects of TC on the isothermal/mixed layer climatology. Summary and discussion are given in section 7.

2. Data

The 6 h best-track data of TCs occurring during 1998–2011 over the northwest Pacific are acquired from the Joint Typhoon Warning Center, which consist of position, maximum sustained surface wind speed, and minimum surface central pressure. Daily precipitation with 1° spatial resolution is obtained from Global Precipitation Climatology Project (GPCP) [*Huffman et al*., 2001]. Daily evaporation data with 1° spatial resolution are from OAFlux [*Yu and Weller*, 2007; *Yu et al*., 2008]. The wind data set is from a new Cross-Calibrated, Multi-Platform (CCMP) ocean surface wind product with a spatial resolution of 0.25° × 0.25° and a temporal resolution of 6 h. The data set is produced by combining all ocean surface wind speed observations from SSM/I, AMSR-E, and TMI, and all ocean surface wind vector observation from QuikSCAT and SeaWinds. Following *Oey et al*. [2006], the wind stress is calculated from the wind field using a bulk formula:

$$\tau=\begin{cases} 0.0012\rho_a\times U_{10}|U_{10}|, & |U_{10}|\le 11\mathrm{ms}^{-1} \\ \rho_a(0.00049+0.000065|U_{10}|)\times U_{10}|U_{10}|, & 11<|U_{10}|\le 19\mathrm{ms}^{-1} \\ \rho_a(0.001364+2.34\times10^{-5}|U_{10}|-2.3\times10^{-7}|U_{10}|^2)\times U_{10}|U_{10}|, & 19<|U_{10}|\le 100\mathrm{ms}^{-1} \end{cases} \quad (1)$$

This formula is modified form *Large and Pond* [1981] to incorporate the limited drag coefficient for high wind speeds [*Powel et al*., 2003].

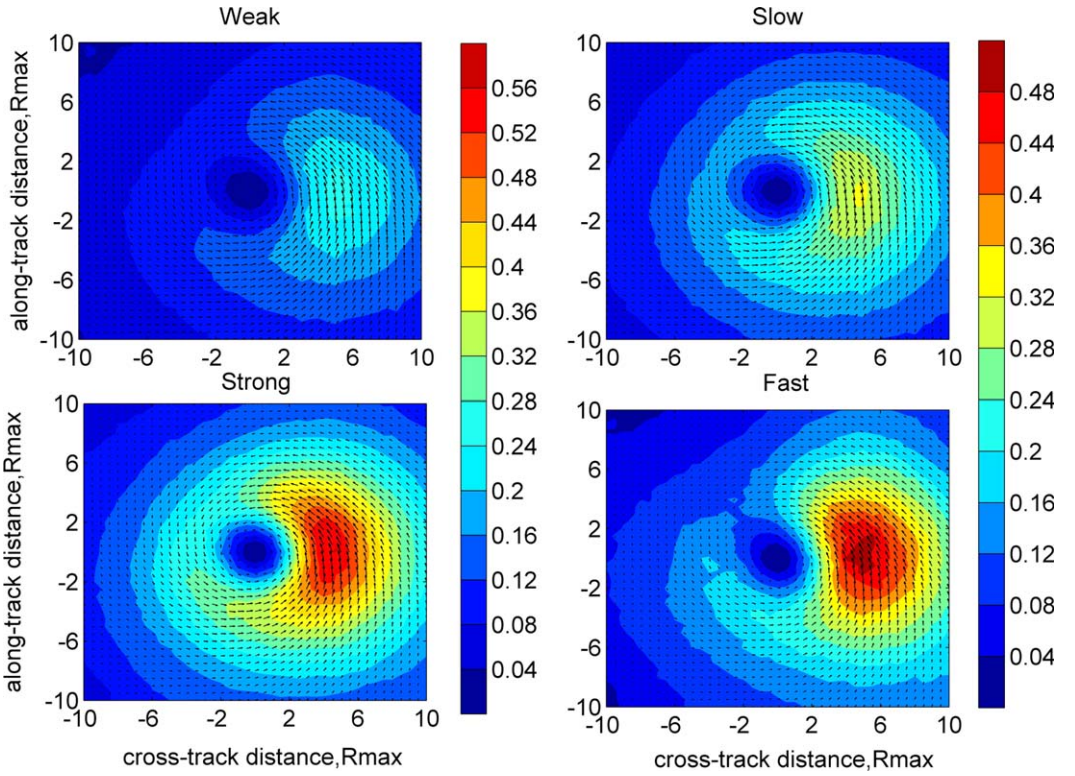

Figure 1. Wind stress magnitudes (color bar) and vectors (black arrow) under weak, strong, slow, and fast TCs. Here R_{max} is the radius of TC's max winds with 47 km as the mean.

In this study, we utilize all the available Argo profiles, from the Coriolis Data Center (ftp://ftp.ifremer.fr), for 1998–2011 in the northwest Pacific. In order to keep data accuracy, real-time and delayed-mode quality controls are performed using the method of *Wong et al.* [2003]. We choose the difference criteria to determine ILD and mixed layer depth (MLD) in the upper ocean from Argo profile data, which requires the deviation of temperature (density) from its upper reference level value to be smaller than a certain fixed value. Since IL or ML is generally deeper than 10 m in the tropical regions, the upper reference level is chosen as 10 m [*Wang et al.*, 2011]. The ILD is defined as a depth at which the temperature is 0.5°C lower than the 10 m depth temperature [*Chu et al.*, 2000b, 2002]. The MLD is corresponding to the depth with density difference $\Delta\sigma_t$ from the upper reference level (here, 10 m level), and the $\Delta\sigma_t$ is calculated as $\Delta\sigma_t = 0.5\frac{\partial\sigma_t}{\partial T}$ at 10 m depth [*Sprintall and Tomczak*, 1992]. The difference between ILD and MLD is defined as barrier layer thickness (BLT).

3. TC Classification

TCs are classified into two groups either by maximum sustained wind speed or translation speed such as weak TCs with maximum sustained wind speed <33 m s^{-1}, and strong TCs with maximum sustained wind speed >33 m s^{-1}, slow TCs with translation speed <7 m s^{-1}, and fast TCs with translation speed >7 m s^{-1}. Since the mean phase speed of the first baroclinic mode in the northwest Pacific is about 2.88 m s^{-1} during summer [*Chang et al.*, 2013], the Froude number F_r, which is the ratio between the translation speed of TCs and the phase speed of first baroclinic mode, is more than 2 for fast TCs, and less than 2 for slow TCs.

The wind stress vectors and magnitudes calculated from CCMP are represented by the matched TC-coordinate systems with the unit vectors in the along-track and cross-track directions. The composite of the wind stress vectors and magnitudes under different types of TCs are shown in Figure 1. The previous study of *Mei et al.* [2012] suggested that storm intensity correlates with translation speed, with hurricanes of category 5 moving on averaged 1 m s^{-1} faster than tropical storm. Figure 1 shows that the wind stress of the fast TCs is stronger than that of the slow TCs. Therefore, our result here roughly agrees with the result of *Mei et al.* [2012]. The left-to-right asymmetric distribution of the wind stress under the fast TCs is clearer compared to the slow TCs.

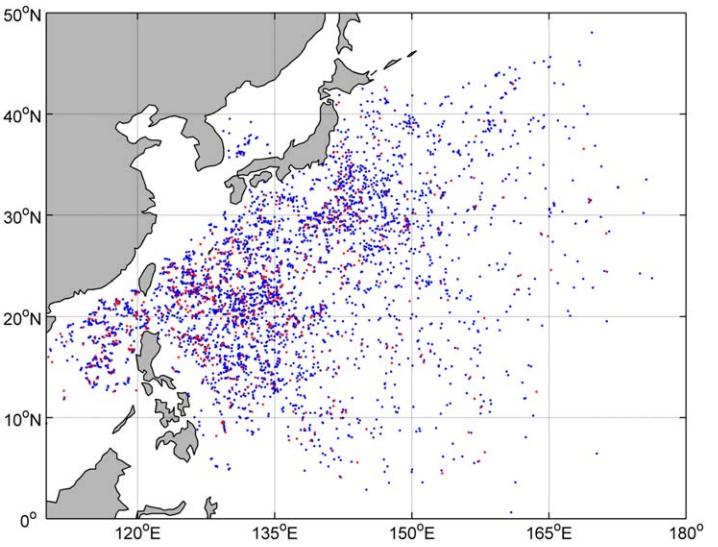

Figure 2. Selected Argo profile pairs used in section 4 (red dots) and section 5 (blue dots).

4. Instantaneous Response of the Mixed Layer

To analyze instantaneous response of upper ocean to different types of TCs, a match-up database is first established between the Argo profile pairs and the TCs in the following three steps: (1) For each TC, the Argo profiles within 500 km radius to its center and within 6 h after the passage are selected. The time selected increment of 6 h equals the temporal resolution of the TC data to avoid a single Argo profile matching to two TCs. (2) The selected Argo profile is paired with another profile taken before the passage of the TC to represent the variation induced by the TC. The maximum distance between the paired is restricted within 50 km [*Wu and Chen*, 2012]. This scale selection is based on a trade-off between the data availability and the closeness of data points to estimate the local response. The maximum time interval between them is restricted to 10 days. (3) The selected Argo profile pairs and corresponding TC are matched up to establish the first database. The red dots in Figure 2 show the distribution of 605 Argo pairs in the database.

Argo profiles from the first database in the Cartesian coordinates also are rotated into the matched TC-coordinate systems. Figure 3 shows the number of profile pairs within 10 times of the radius of maximum wind (R_{max}) in the cross-track and the along-track directions. The R_{max} with 47 km is the mean of the radius of TC's maximum winds [*Hsu and Yana*, 1998]. In the most area, the slow TCs usually have the most profile pairs in all of the four groups. In contrast, the fast TCs generally have the least profile pairs. The ILD, MLD, BLT, and ILT can be obtained from Argo profiles, and their variability during TC passage is calculated as the difference between the Argo profile pairs to represent real-time responses of the mixed layer to TCs. Figure 4 gives the statistical characteristic of changes for the ILD, MLD, BLT, and ILT under the different types of TCs. The uncertainty is estimated by the standard deviation divided by the root mean square of the number of profile pairs in each bin [*Wu and Chen*, 2012]. The uncertainties in the inner core of all TCs except for the fast TCs are small. The large uncertainty away from the TC center and under fast TCs may be related to fewer samples (Figure 5).

The net freshwater flux is obtained from daily evaporation and precipitation during the period from the 1 day before TC passage to the day of TC occurrence, which is shown by the black contours in Figure 4. The rightward biases of the IL and ML deepening and IL cooling are more obvious during strong TCs than during weak TCs. The magnitude and extent of the IL deepening induced by strong TCs are larger than those induced by weak TCs. The maximum IL deepening on the right side of the strong TC's center is above 15 m. The magnitude of ML deepening induced by the strong TCs is larger in the most area except for the area with large net freshwater flux compared to weak TCs. The reduction of ILT on the right side of strong TC's center is usually larger than that to the weak TC's center, with extensive coverage (Figure 4).

Similarly, the magnitude of the IL deepening on the right side of the fast TCs is larger than that on the right side of the slow TCs (Figure 4), which may be related to the stronger wind stress on the right side of the fast TCs (Figure 1). MLD changes are not completely coherent with the ILD changes. The ML deepening on the right side is larger for the slow TCs than for the fast TCs. Like ILD, the stronger wind stress on the right side of the fast TCs supports that the isothermal layer cooling induced by the fast TCs is wider than that induced by the slow TCs (Figure 4).

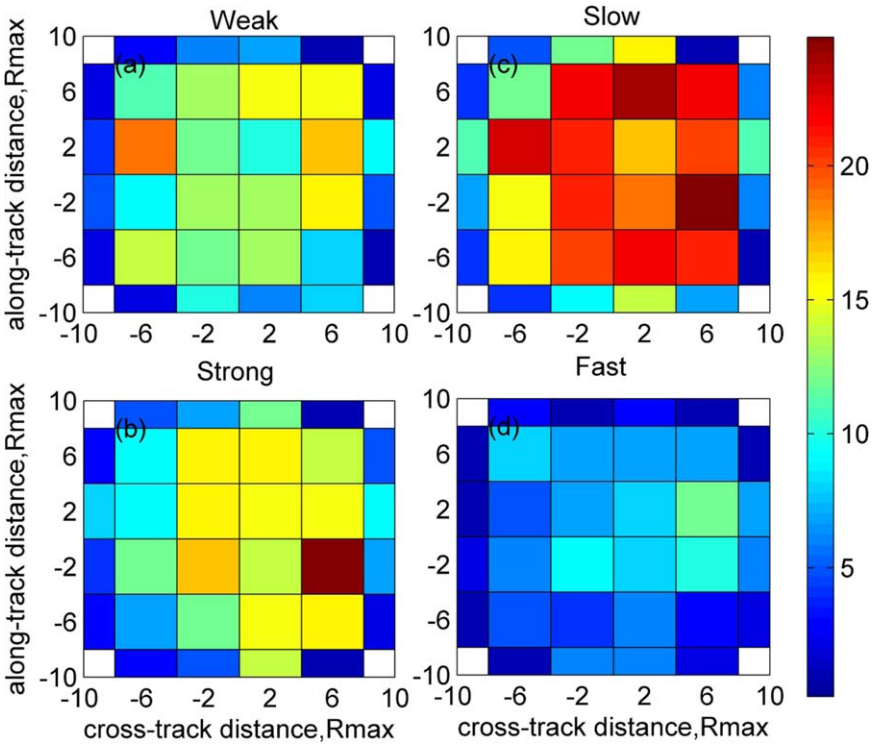

Figure 3. Number of profile pairs used in section 4 for the (a) weak, (b) strong, (c) slow, and (d) fast TCs. Here R_{max} is the radius of TC's max winds with 47 km as the mean.

In the TC inner core (i.e., within about 100 km of the TC center), the net freshwater fluxes under the strong and slow TCs are much larger than those under the weak and fast TCs. For strong and slow TCs, the corresponding BLT in the area with large net freshwater flux increases rapidly. The positive buoyancy flux of the TC-induced rainfall can affect static stability of the ocean mixed layer, with the ability to restrain the vertical mixing. Thus, the TC-induced rainfall tends to make ML shoal and in turn to increase BLT.

The impact of the initial BLT prior to TC on the instantaneous response of ILT is analyzed by the linear regression based on the Argo profile pairs within the radius of 200 km from TC centers (Figure 6). The initial BLT is positively correlated with the ILT change with the 95% confidence level, indicating that the initial BL can restrain the IL cooling [*Wang et al*., 2011]. The correlation coefficient between the initial BLT and ILT change for the strong TCs is smaller than that for the weak TCs. This is because more vigorous vertical mixing and upwelling induced by strong wind may more easily overcome the haline stratification to entrain the cold thermocline water. Compared with the fast TCs, the longer residence of the vertical mixing and upwelling under the slow TCs tend to support a smaller correlation coefficient between the initial BLT and ILT change.

5. Temporal and Spatial Variability of the Mixed Layer Response

To examine evolution of the mixed layer response to TCs, the second match-up database is established between Argo profile pairs and TCs by the following step: (1) for each Argo profile, it will be selected if there is TC occurrence within the 500 km away from the profile and within 10 day before the observation of the profile, and the selected Argo profile is matched with the spatially closest TC; (2) the selected Argo profile is paired by the similar method used to establish the first database in section 4; (3) the Argo pairs and matched TC are used to establish the second database. The blue dots in Figure 1 show the distribution of 3927 Argo pairs in the second database.

Based on the second database, the spatial-temporal variability of the mixed layer response under different types of TCs is examined with highly varying spatial-temporal distributions of the profile pair number from 40 to 5 in each bin (Figure 7). The spatial-temporal distribution of ILD, MLD, BLT, ILT changes after TC

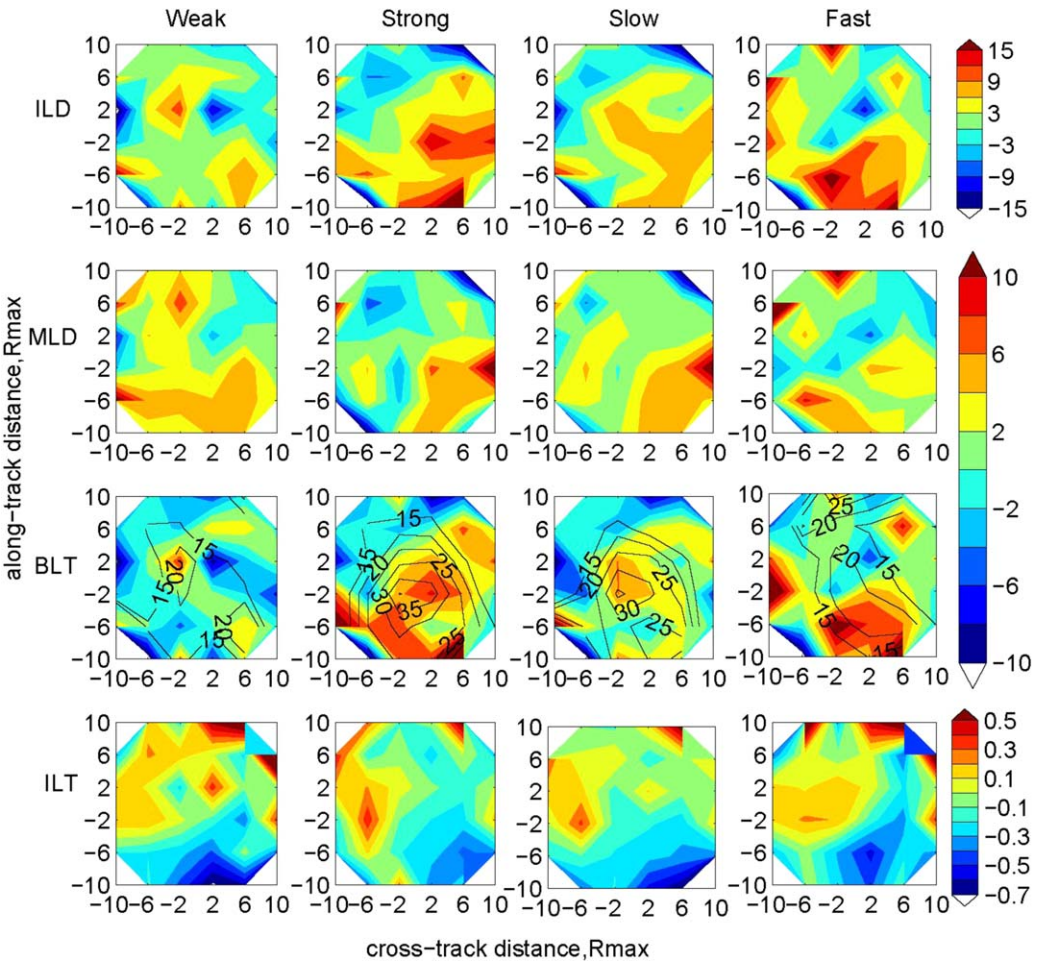

Figure 4. Instantaneous response of the ILD (m), MLD (m), BLT (m), and ILT (°C) during the weak, strong, slow, and fast TCs. Black contour indicates the averaged net freshwater flux (mm/d) from the 1 day before TC occurrence to the day of TC occurrence. Here R_{max} is the radius of TC's max winds with 47 km as the mean.

passage are given in Figure 8. For weak TCs, there are no obvious rightward biases of IL, ML deepening and IL cooling during about 10 days after TC passage (Figure 8). At the third to fourth days after weak TC passage, within the radius of 200 km the IL and ML deepen, and the IL cools (Figure 8). Such change is more evident under the strong TCs than under weak TCs. The ML shoaling within 100 km of the strong TC centers is much clearer, which may result from the vigorous upwelling in the region of the TC inner core. The associated IL cooling under the strong TC has more evident rightward bias. The maximum IL cooling can reach up to about 1°C near the strong TC's center (Figure 8).

Besides, the rightward bias of IL deepening is more evident induced by the fast TCs than by the slow TCs, which is attributed to the stronger left-right asymmetry distribution of the wind stress under fast TCs (Figure 1). The ML shoaling near the inner core of the slow TC is clearer than that near the inner core of the fast TC as the result of strong upwelling. Compared to the fast TCs, the temporal-spatial distribution of IL cooling induced by the slow TCs presents a left-right symmetry character with the maximum cooling near the TC's center, which indicates the important role of upwelling (Figure 8).

Previous studies showed that the Froude number F_r determines the forms of the upper-ocean response: upwelling or near-inertial wave wakes [*Geisler*, 1970; *Nilsson*, 1995]. If $F_r \gg 1$, the baroclinic response with the near-inertial waves plays a dominant role, whereas ocean response tends to be barotropic response with the upwelling in the storm centers when F_r becomes to smaller and smaller. Thus, the mixed layer response to the slow TCs with $F_r < 2$ may be dominated by the stronger upwelling.

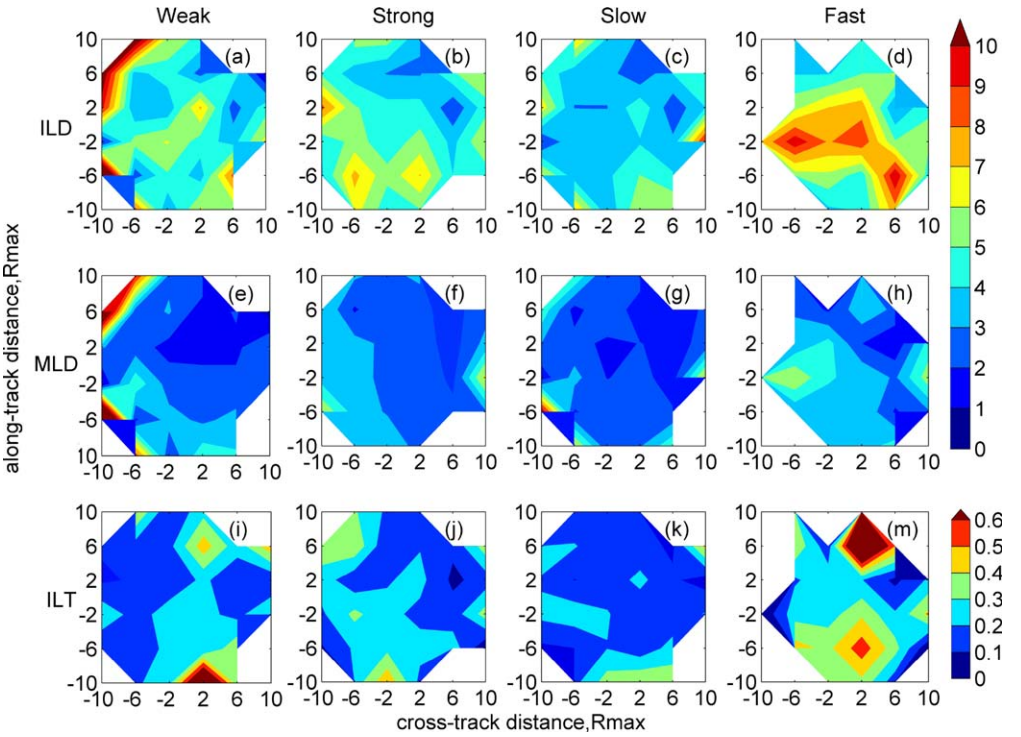

Figure 5. Uncertainty of ILD (m), MLD (m), and ILT (°C) changes during the weak, strong, slow, and fast TCs, which is calculated by the standard deviation divided by the root mean square of the number of profile pairs. Here R_{max} is the radius of TC's max winds with 47 km as the mean.

The uncertainty is also estimated by the standard deviation divided by the root mean square the number of profile pairs in each bin (Figure 9). The uncertainties of ILD, MLD, ILT changes in most area are small, with mean values of 4.0 m, 2.3 m, and 0.25°C, respectively. The large uncertainty is mainly associated with few Argo profile samples.

Figure 10 shows the radial dependence of the azimuthally averaged ILT and ILD changes within 10 day after TC passage for the weak, strong, slow, and fast TCs. ILT and ILD variability under the weak TCs is relatively small (Figure 10a). The IL deepening induced by the strong TCs has a maximum of 8 m at about 150 km of

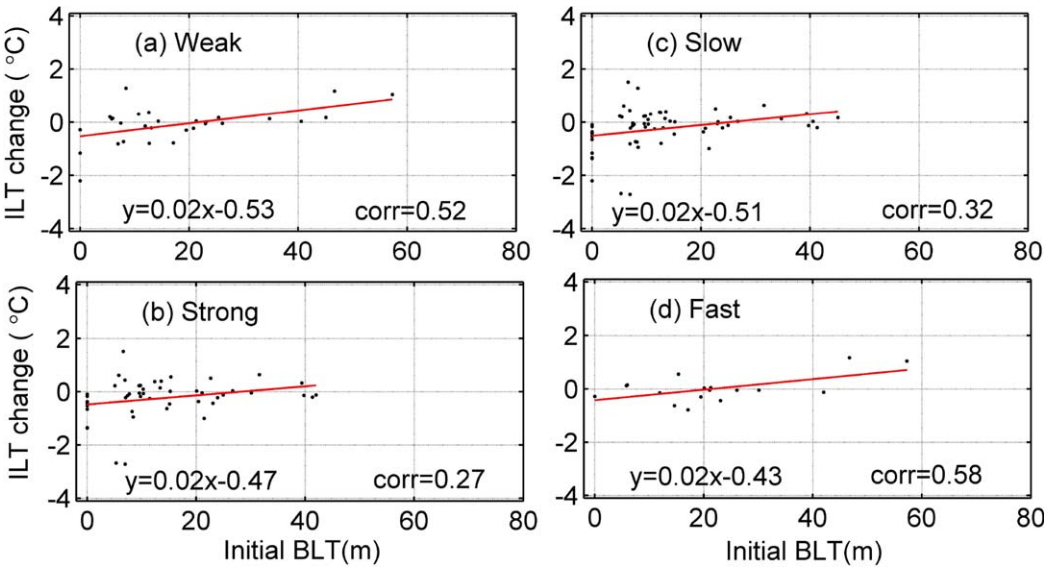

Figure 6. Relationships between initial barrier layer thickness (m) and ILT changes (°C) within the radius of 200 km for the weak, strong, slow, and fast TC.

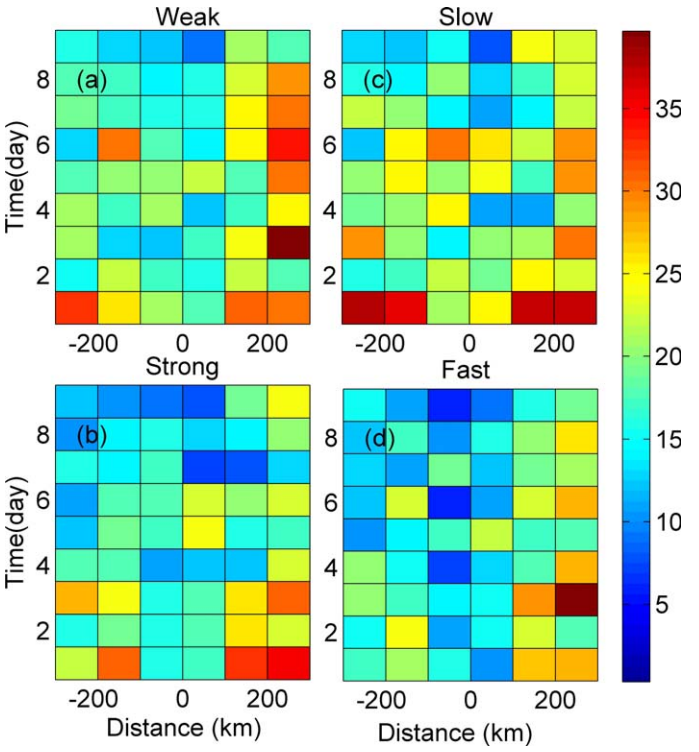

Figure 7. Time-space (radial) plots of the azimuthally averaged profile pairs for the (a) weak, (b) strong, (c) slow, and (d) fast TCs. The positive (negative) sign of the horizontal axis indicates right (left) side of the along-track direction. The unit of time is the day after TCs passage.

the right side of the along-track direction. It is noted that the strong IL deepening is also found at about 150 km of the left side. This may be caused by the passage of TCs over the ocean leaving behind the strong inertial oscillations and thus leading to the formation of convergence and divergence zones [*Ginis*, 2002; *Rao et al.*, 2010; *Wang et al.*, 2014]. The maximum IL cooling of about 0.6°C induced by the strong TCs is situated at 50 km of the right of the TC track, where the IL deepening reaches minimum as a result of the vigorous upwelling (Figure 10b). Compared with the ILD change, the ILT change exhibits a more obvious asymmetry with more cooling on the right side of the strong TC track, which may be related to the existence of both TC-induced vertical mixing and upwelling mechanisms.

The ILT and ILD changes induced by the slow TCs show the strongly positive correlation with the correlation coefficient of 0.77 on the 95% confidence level (Figure 10c). Generally, the TC-induced vertical mixing can make IL deepen whereas the TC-induced upwelling can make IL shoal. Besides, both mechanisms can make IL cool. Thus, the positive correlation suggests a dominant role played by the Ekman pumping under the slow TCs. However, the correlation between the ILT and ILD change induced by the fast TCs is out-of-phase, with the correlation coefficient of −0.70 which is statistically significant at the 95% confidence level. This negative correlation under the fast TCs indicates the dominance role of the mixing process.

Time evolutions of the averaged ILT and ILD changes within the radius of 100 km for the weak, strong, slow, and fast TCs clearly show the inertial oscillation induced by TC passage with three minima of the ILT changes within 10 day for each TC type (Figure 11). Comparing with the weak TCs, ILD, and ILT changes show larger amplitude within 4–10 days after the strong TC passages, indicating that the inertial oscillation induced by the strong TCs can persist for a longer time. Figure 11b shows that the IL cooling lags 1 day behind the IL deepening after the strong TC passage. The lagged correlation coefficient between the ILT and ILD changes is −0.84, which is statistically significant at the 95% confidence level. The amplitudes of the ILT and ILD changes are smaller within 1–5 days induced by the slow TCs than by the fast TCs, indicating the stronger inertial oscillation after the fast TC passages. The ILT and ILD sharply reduce within 8–10 days after the fast TC passages. Just as the instantaneous response, the relationship between the initial BLT and the ILT change is also analyzed by linear regression within 10 days after TC passages (Figure 12). The correlation coefficients between the initial BLT and the ILT change are all positive for the weak, strong, slow, and fast TCs. It also proves that the initial BL can weaken IL cooling.

6. Effect of TCs on the Mixed Layer Climatology

Since TCs pronouncedly occur in July to October, the Argo profiles are selected to investigate the effect of TCs on the mixed layer during July to October. The Argo profiles are separated into two groups. The first group includes all the Argo profiles in July to October during 1998–2011, whereas the second group

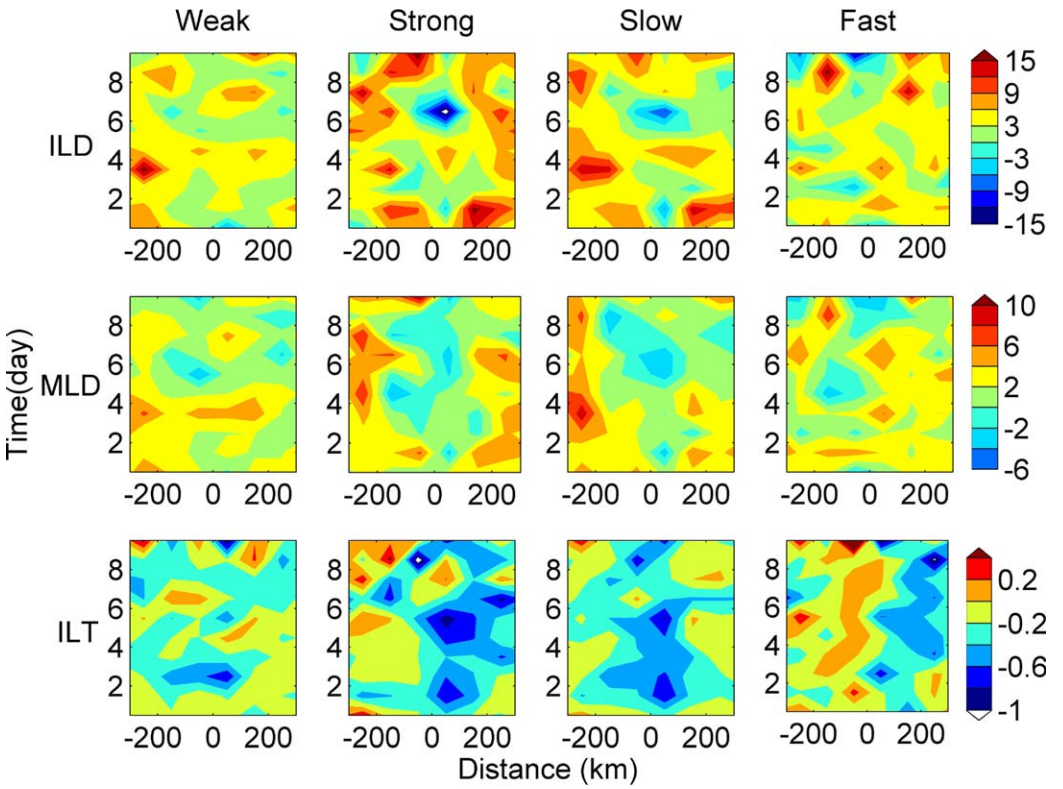

Figure 8. Time-space (radial) plots of the azimuthally averaged ILD (m), MLD (m), BLT (m), and ILT (°C) changes induced by the weak, strong, slow, and fast TCs. The positive (negative) sign of the horizontal axis indicates right (left) side of the along-track direction. The unit of time is the day after TCs passage.

excludes the Argo profiles influenced by TCs. The number of Argo profiles in 3° × 3° grid cells for each of two groups is shown in Figures 13a and 13b, and the difference between two groups is given in Figure 13c. More than 50 Argo profiles are available in each bin with above 150 Argo profiles near the Kuroshio for each of two groups. The Argo profiles under the influence by TCs are mainly located in the area of 120°–140° longitudes and 15°–35° latitudes where TCs frequently occur (Figure 13c).

Based on all the Argo profiles during 1998–2011, the means of ILD, MLD, and ILT in 3° × 3° grid cells are calculated to present the spatial distribution of climatology in July to October (Figure 14). The MLD reduces northward and southward from 45 m in the zonal band of 10°N–20°N to less than 25 m at high latitudes. The ILT decreases gradually from low to high latitudes with much higher than 29°C at low latitudes, and less than 17°C at high latitudes (north of 40°N). The spatial distributions of climatological ILD, MLD, and ILT obtained from the first Argo profile group are consistent with the previous studies [e.g., *Chang et al.*, 2009].

Figure 15 shows the differences of climatological ILD, MLD, and ILT between the first and second groups. Figure 16 shows the number of TC occurrence and the averaged maximum sustained wind speed in 3° × 3° grid cells during 1998–2011. Under the TC influence, the IL and ML deepen up to 5 m in the subtropical gyre of the northwest Pacific (125°E–155°E, 20°N–40°N). The averaged maximum sustained wind speeds are much larger than those in other areas, which indicate stronger TC-induced mixing (Figure 16b). Actually, the most pronounced vertical diffusivity induced by TCs situates in this region [*Sriver and Huber*, 2007]. The associated IL cooling induced by TCs in the TC-active region is more than 0.12°C, with the maximum cooling of about 0.4°C. However, the IL and ML become shallow and IL cooling becomes weak, even warming in the outer edge of TC-active region, for example, in the most area of (140°E–165°E, 5°N–25°N) where the probability of TC passage is very low. The positive wind stress curl in the TC-active region causes the upwelling and horizontal divergence, and in turn produce the downwelling and horizontal convergence in the outside edge of the TC-active region. Our results also support that the TC-winds can strengthen climatological background Ekman pumping [*Jullien et al.*, 2012; *Scoccimarro et al.*, 2011].

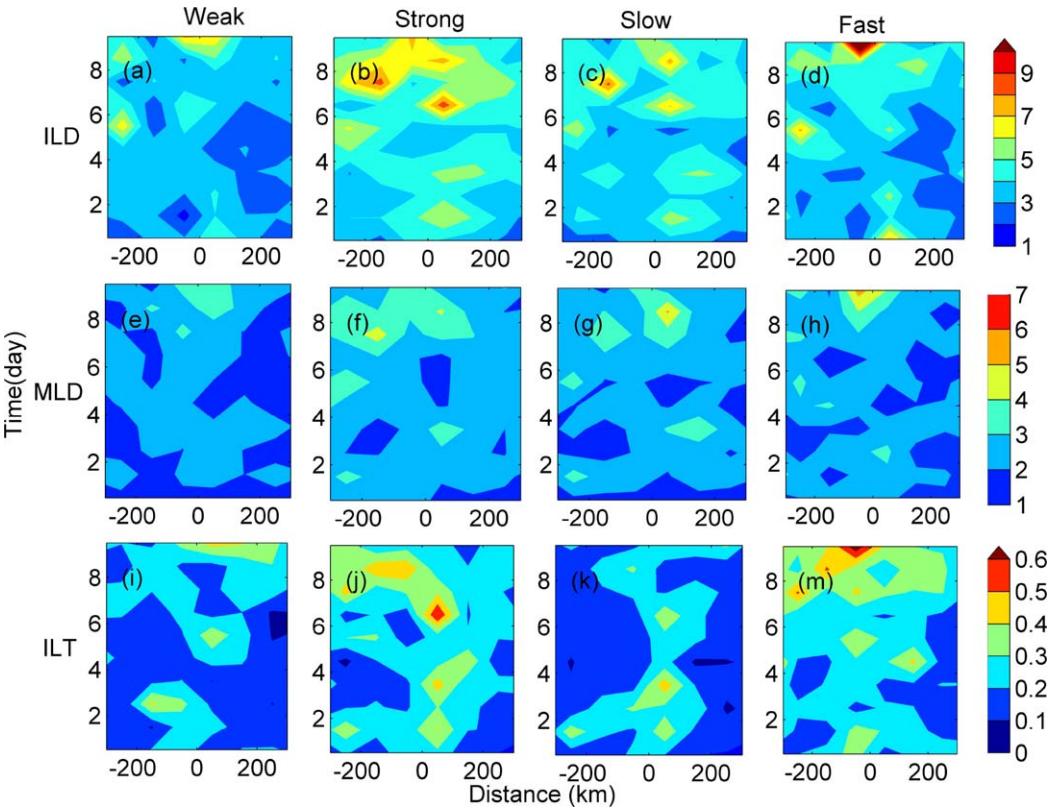

Figure 9. Time-space (radial) plots of uncertainty of the azimuthally averaged ILD (m), MLD (m), BLT (m), and ILT (°C) changes induced by the weak, strong, slow, and fast TCs. The positive (negative) sign of the horizontal axis indicates right (left) side of the along-track direction. The unit of time is the day after TCs passage.

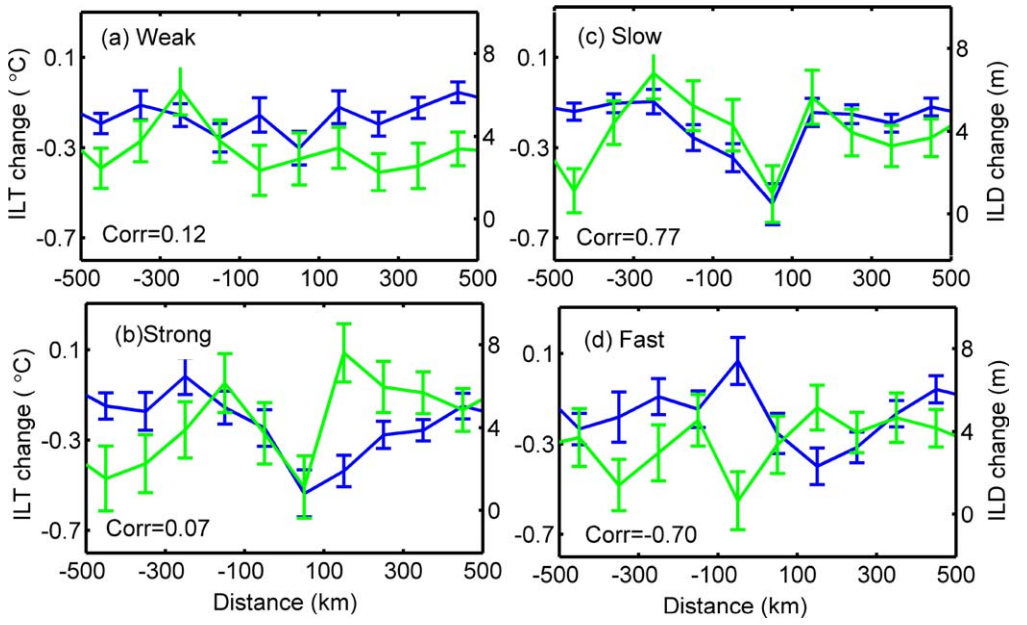

Figure 10. Radial dependence of the azimuthally averaged ILT (blue line, °C) and ILD (green line, m) changes within 10 days after TC passage under the weak, strong, slow, and fast TCs. The positive (negative) sign of the horizontal axis indicates right (left) side of the along-track direction. The error bar with ±1 standard deviation indicates the estimated uncertainty.

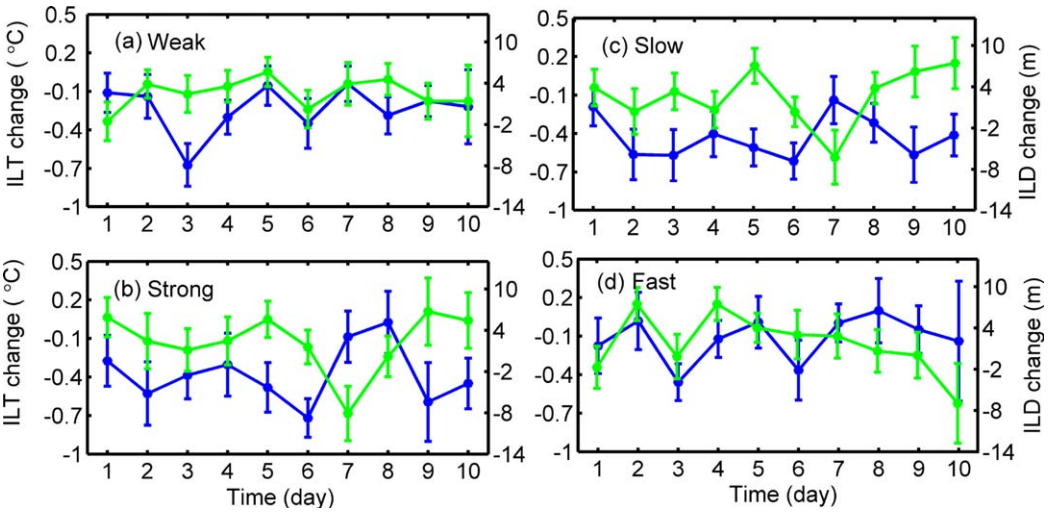

Figure 11. Time evolution of the averaged ILT (blue line, °C) and ILD (green line, m) changes within the radial distance of 100 km under the weak, strong, slow, and fast TCs. The error bar with ±1 standard deviation indicates the estimated uncertainty.

7. Summary and Discussion

Based on the historical data (1998–2011) of Argo profiles, TCs, CCMP winds, evaporation, and precipitation, the characteristics of the mixed layer response to different types of TCs have been obtained in this study for the northwest Pacific. The main conclusions are given as follows.

1. The instantaneous response of the mixed layer to the different types of TCs is investigated. Compared to the weak TCs, the rightward biases of IL and ML deepening and IL cooling are more evident during the strong TCs as a result of the more obvious rightward biased distribution of wind stress under the strong TCs. It is demonstrated from the observation that the heavy rainfall in the inner core of the strong and slow TCs tend to make ML shoal, and therefore BL thicken. Similarly, the magnitudes of IL deepening and IL cooling on the right side of the fast TCs with stronger wind stress are larger than that of the slow TCs. It is more obvious that the initial BL prior to TC passage restrains the IL cooling under the weak and fast TCs, relative to the strong and slow TCs.

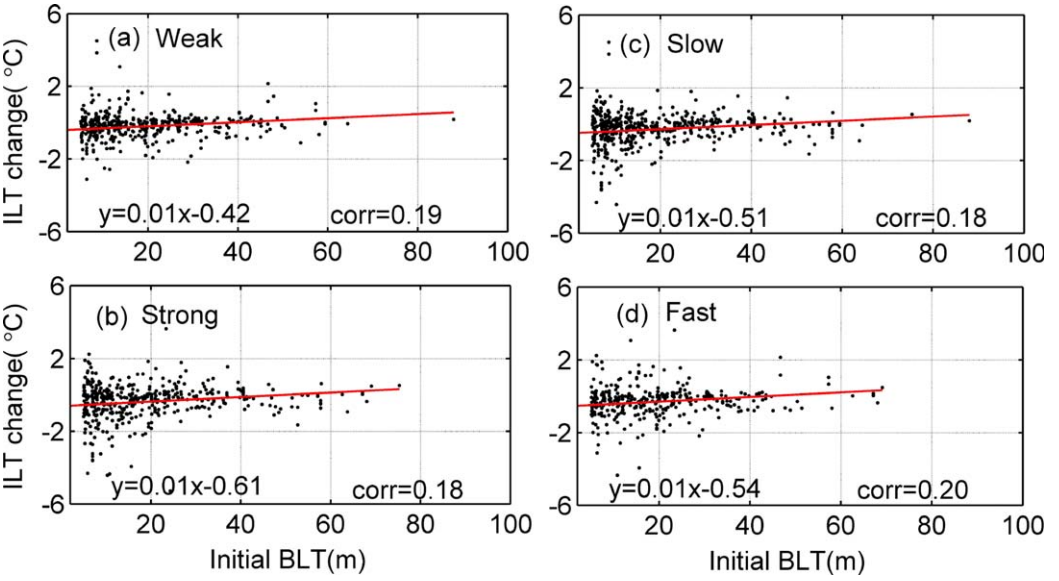

Figure 12. Relationship between initial barrier layer thickness (m) and ILT changes (°C) under (a) the weak, (b) strong, (c) slow, and (d) fast TC. The Argo profile pairs within the radial distance of 200 km from the TC's centers and 10 days after the TC passage are used.

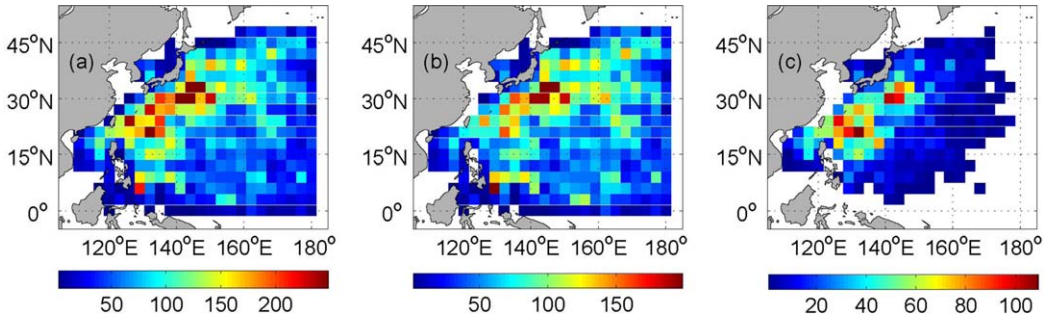

Figure 13. Number of (a) all the Argo profiles, (b) the Argo profiles excluding that influenced by TCs, and (c) the Argo profiles influenced by TCs in the 3° × 3° grid cells during 1998–2011.

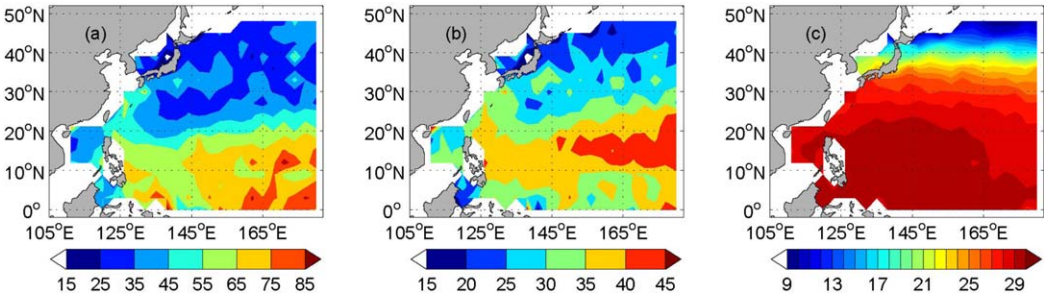

Figure 14. Climatological mean of (a) ILD (m), (b) MLD (m), and (c) ILT (°C) from all the Argo profiles during July to October of 1998–2011 with 3° × 3° resolution.

2. The temporal-spatial variability of the mixed layer response to the different types of TCs is explored. Comparing with the weak TCs, the variability of the ILD, MLD, and ILT is stronger within 10 days after the strong TC passage, with strong upwelling in the inner cores. The rightward biases of IL and ML deepening and IL cooling induced are more evident and the upwelling in their inner cores induced is weaker by fast TCs than by slow TCs, which may be attributed to the stronger left-right asymmetry distribution of wind stress and faster translation under the fast TCs. The mixed layer response is dominated by the Ekman pumping for the slow TCs, whereas by the mixing process for the fast TCs. The ILT and ILD changes within the radius of 100 km for all the TCs show the inertial oscillation with larger amplitudes under strong/fast TCs than under weak/slow TCs. Furthermore, the IL cooling lags 1 day behind the IL deepening within the radius of 100 km from strong TC centers.
3. The TC effect on mixed layer climatology during July to October is studied. The TCs act to deepen the climatological ILD and MLD, and cool the ILT in the area with frequent TC passages. The most pronounced IL, ML deepening, and IL cooling occur in the subtropical gyre of the northwest Pacific (125°E–155°E, 20°N–40°N) where strong vertical diffusivity is induced by TCs. The maximum IL and ML deepening is up to 5 m, with IL cooling up to 0.4. Nevertheless, it is also found that the IL and ML become shallow and the IL cooling becomes weak, even warming in the outer edge of TC-active region. It is mainly caused by

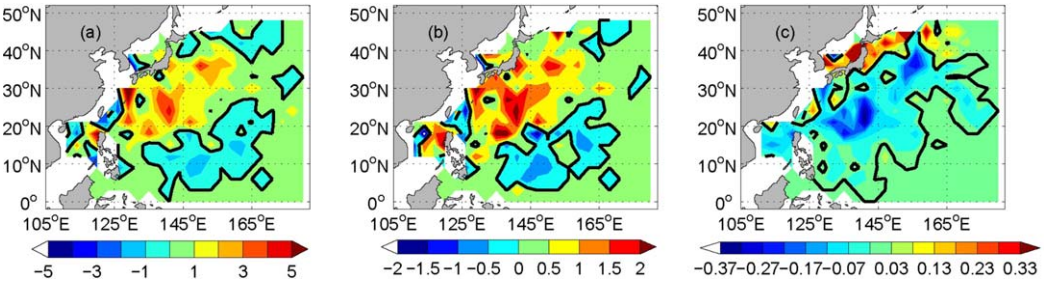

Figure 15. Differences of (a) the ILD (m), (b) MLD, and (c) ILT (°C) between all the Argo profiles and the Argo profiles under no influence of TCs during July to October of 1998–2011 with 3° × 3° resolution.

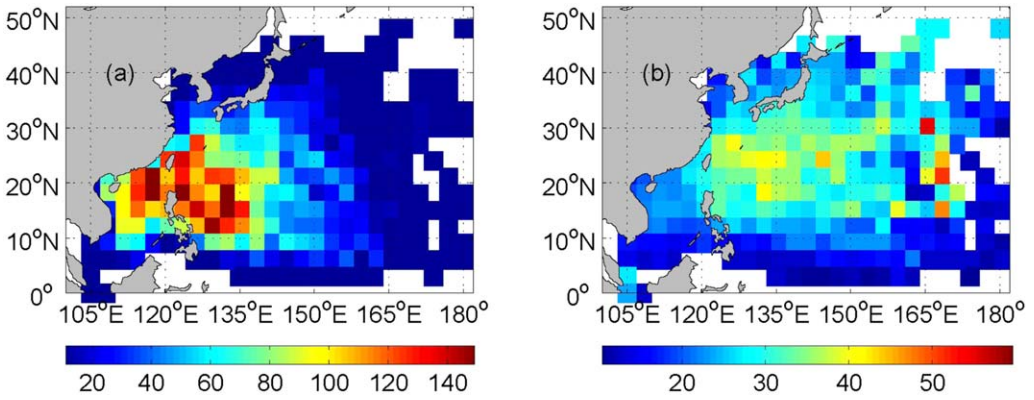

Figure 16. Horizontal distributions of (a) total number of 6 h occurrence of TCs, and (b) averaged maximum sustained wind speed (m/s) in 3° × 3° grid cells during 1998–2011.

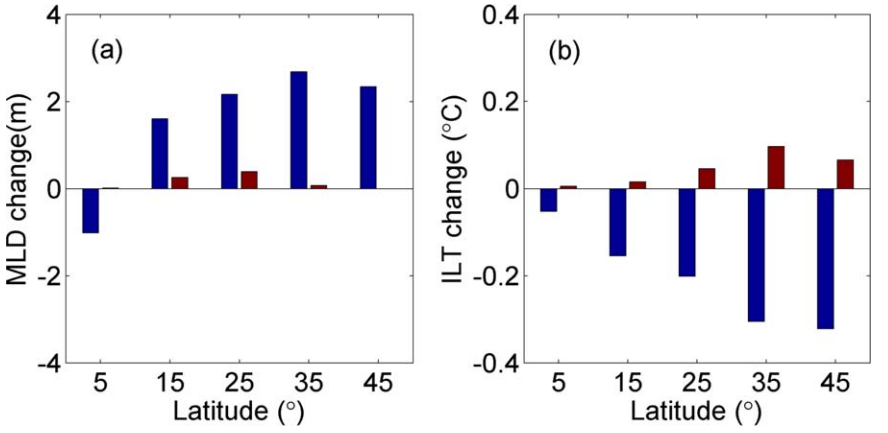

Figure 17. Latitudinal distribution of averaged (a) MLD and (b) ILT changes (m) from Argo profile pairs under no influence of TCs (red) and under the influence of TCs (blue).

the upwelling and horizontal divergence due to positive wind stress curl in the TC-active region, and in turn, to balance the water mass, the downwelling and horizontal convergence occur in the outside edge of the TC-active region.

When we analyze the mixed layer changes between after the TC passage and before the TC passage, the statistical method may have some uncertainty, which mainly result from sampling errors and oceanic background variability. The sampling error has been given and discussed. Here the uncertainty caused by the background variability is given and discussed. All Argo profiles of 1998–2011 are divided into two groups according to whether they are influenced by TCs or not. For each group, Argo profiles are also paired by the similar method in section 4 and the changes of the MLD and ILT are calculated based on Argo profile pairs. The averaged MLD and ILT changes under non-TC and TC influence are given, respectively (Figure 17). Though the oceanic background MLD changes at 10°N–30°N and ILT changes at 30°N–50°N are larger than those at other latitudes, they are far less than the TC-induced changes. Thus, the results in the study can represent the characteristics of the mixed layer response to the TCs with a permissible uncertainty.

Acknowledgments
This study was supported by the National Basic Research Program of China (2013CB430304), National Natural Science Foundation (41030854, 41106005, 41176003, 41206178, and 41376015) of China, and National High-Tech R&D Program (2013AA09A505) of China. Peter C. Chu was supported by the Office of Naval Research and Naval Oceanographic Office.

References

Balaguru, K., P. Chang, R. Saravanan, L. R. Leung, Z. Xu, M. K. Li, and J. S. Hsieh (2012), Ocean barrier layers' effect on tropical cyclone intensification, *Proc. Natl. Acad. Sci. U. S. A.*, *109*, 14343–14347, doi:10.1073/pnas.1201364109.

Chang, S., and R. Anthes (1978), Numerical simulations of the ocean's nonlinear baroclinic response to translating hurricanes, *J. Phys. Oceanogr.*, *8*, 468–480.

Chang, S. W. (1985), Deep ocean response to hurricanes as revealed by an ocean model with free surface. Part I: Axisymmetric case, *J. Phys. Oceanogr.*, *15*, 1847–1858.
Chang, Y. C., G. Y. Chen, R. S. Tseng, L. R. Centurioni, and P. C. Chu (2012), Observed near-surface currents under high wind speeds, *J. Geophys. Res.*, *117*, C11026, doi:10.1029/2012JC007996.
Chang, Y. C., G. Y. Chen, R. S. Tseng, L. R. Centurioni, and P. C. Chu (2013), Observed near-surface flows under all tropical cyclone intensity levels using drifters in the northwestern Pacific, *J. Geophys. Res. Oceans*, *118*, 2367–2377, doi:10.1002/jgrc.20187.
Chang, Y. S., A. J. Rosati, S. Q. Zhang, and M. J. Harrison (2009), Objective analysis of monthly temperature and salinity for the world ocean in the 21st century: Comparison with World Ocean Atlas and application to assimilation validation, *J. Geophys. Res.*, *114*, C02014, doi:10.1029/2008JC004970.
Chu, P. C., and C. W. Fan (2010), Optimal linear fitting for objective determination of ocean mixed layer depth from glider profiles, *J. Atmos. Oceanic Technol.*, *27*, 1893–1898.
Chu, P. C., and C. W. Fan (2011), Maximum angle method for determining mixed layer depth from seaglider data, *J. Oceanogr.*, *67*, 219–230.
Chu, P. C., and G. H. Wang (2003), Seasonal variability of thermohaline front in the central South China Sea, *J. Oceanogr.*, *59*, 65–78.
Chu, P. C., S. H. Lu, and W. T. Liu (1999), Uncertainty of the South China Sea prediction using NSCAT and NCEP winds during tropical storm Ernie 1996, *J. Geophys. Res.*, *104*, 11,273–11,289.
Chu, P. C., J. M. Veneziano, C. W. Fan, M. J. Carron, and W. T. Liu (2000a), Response of the South China Sea to tropical cyclone Ernie 1996, *J. Geophys. Res.*, *105*, 13,991–14,009.
Chu, P. C., C. W. Fan, and W. T. Liu (2000b), Determination of vertical thermal structure from sea surface temperature, *J. Atmos. Oceanic Technol.*, *17*, 971–979.
Chu, P. C., Q. Y. Liu, Y. L. Jia, and C. W. Fan (2002), Evidence of barrier layer in the Sulu and Celebes Seas, *J. Phys. Oceanogr.*, *32*, 3299–3309.
Cione, J. J., and E. W. Uhlhorn (2003), Sea surface temperature variability in hurricanes: Implications with respect to intensity change, *Mon. Weather Rev.*, *131*, 1783–1795.
Emanuel, K. A. (1991), The theory of hurricanes, *Annu. Rev. Fluid Mech.*, *23*, 179–196.
Emanuel, K. A. (2001), Contribution of tropical cyclones to meridional heat transport by the oceans, *J. Geophys. Res.*, *106*, 14,771–14,781.
Fedorov, A. V., C. M. Brierley, and K. A. Emanuel (2010), Tropical cyclones and permanent El Niño in the early Pliocene epoch, *Nature*, *463*, 1066–1070.
Geisler, J. E. (1970), Linear theory of the response of a two-layer ocean to a moving hurricane, *Geophys. Fluid Dyn.*, *1*, 249–272.
Ginis, I. (2002), Tropical cyclone-ocean interactions, in *Atmosphere-Ocean Interactions, Adv. Fluid Mech. Ser.*, vol. 33, edited by W. Perrie, chap. 3, pp. 83–114, WIT Press, Southampton, U. K.
Ginis, I., and G. Sutyrin (1995), Hurricane-generated depth-averaged currents and sea surface elevation, *J. Phys. Oceanogr.*, *25*, 1218–1242.
Hart, R. E., R. N. Maue, and M. C. Watson (2007), Estimating local memory of tropical cyclones through MPI anomaly evolution, *Mon. Weather Rev.*, *135*, 3990–4005.
Hsu, S. A., and Z. Yana (1998), A note on the radius of maximum winds for hurricanes, *J. Coastal Res.*, *12*, 667–668.
Hu, A., and G. A. Meehl (2009), Effect of the Atlantic hurricanes on the oceanic meridional overturning circulation and heat transport, *Geophys. Res. Lett.*, *36*, L03702, doi:10.1029/2008GL036680.
Huffman, G. J., R. F. Adler, M. Morrissey, D. T. Bolvin, S. Curtis, R. Joyce, B. McGavock, and J. Susskind (2001), Global precipitation at one-degree daily resolution from multi-satellite observations, *J. Hydrometeorol.*, *2*, 36–50.
Jacob, S. D., L. K. Shay, and A. J. Mariano (2000), The 3D oceanic mixed layer response to Hurricane Gilbert, *J. Phys. Oceanogr.*, *14*, 59–78.
Jaimes, B., and L. K. Shay (2010), Near-inertial wave wake of hurricanes Katrina and Rita over mesoscale oceanic eddies, *J. Phys. Oceanogr.*, *40*, 1320–1337.
Jullien, S., C. E. Menkes, P. Marchesiello, N. C. Jourdain, M. Lengaigne, A. Koch-Larrouy, J. Lefèvre, E. M. Vincent, and V. Faure (2012), Impact of tropical cyclones on the heat budget of the South Pacific Ocean, *J. Phys. Oceanogr.*, *42*, 1882–1905.
Large, W. G., and S. Pond (1981), Open ocean flux measurements in moderate to strong winds, *J. Phys. Oceanogr.*, *2*, 218–224.
Liu, H. L., S. A. Grodsky, and J. A. Carton (2009), Observed subseasonal variability of oceanic barrier and compensated layers, *J. Clim.*, *22*, 6104–6119, doi:10.1175/2009JCLI2974.1.
Liu, L. L., W. Wang, and R. X. Huang (2008), The mechanical energy input to the ocean induced by tropical cyclones, *J. Phys. Oceanogr.*, *38*, 1253–1266.
Liu, Z., J. Xu, B. Zhu, C. Sun, and L. Zhang (2007), The upper ocean response to tropical cyclones in the northwestern Pacific analyzed with Argo data, *Chin. J. Oceanol. Limnol.*, *25*(2), 123–131, doi:10.1007/s00343-007-0123-8.
Mei, W., C. Pasquero, and F. Primeau (2012), The effect of translation speed upon the intensity of tropical cyclones over the tropical ocean, *Geophys. Res. Lett.*, *39*, L07801, doi:10.1029/2011GL050765.
Nam, S. H., D. J. Kim, and W. M. Moon (2011), Observed impact of mesoscale circulation on oceanic response to Typhoon Man-Yi (2007), *Ocean Dyn.*, *62*(1), 1–12, doi:10.1007/s10236-011-0490-8.
Nilsson, J. (1995), Energy flux from traveling hurricanes to the oceanic internal wave field, *J. Phys. Oceanogr.*, *25*, 558–573.
Oey, L. Y., T. Ezer, D. P. Wang, S. J. Fan, and X. Q. Yin (2006), Loop current warming by hurricane Wilma, *Geophys. Res. Lett.*, *33*, L08613, doi:10.1029/2006GL025873.
Park, J. J., K. A. Park, K. Kim, and Y. H. Youn (2005), Statistical analysis of upper ocean temperature response to typhoons from ARGO floats and satellite, in *Geoscience and Remote Sensing Symposium, IGARSS '05 Proceedings*, vol. 4, pp. 2564–2567, IEEE, Seoul.
Powel, M., P. Vickery, and T. Reinhold (2003), Reduced drag coefficients for high wind speeds in tropical cyclones, *Nature*, *422*, 279–283.
Price, J. F. (1981), Upper ocean response to a hurricane, *J. Phys. Oceanogr.*, *11*, 153–175.
Price, J. F., T. B. Sanford, and G. Z. Forristall (1994), Forced stage response to a moving hurricane, *J. Phys. Oceanogr.*, *24*, 233–260.
Rao, A. D., J. Madhu, I. Jain, and M. Ravichandran (2010), Response of subsurface waters in the eastern Arabian Sea to tropical cyclones, *Estuarine Coastal Shelf Sci.*, *89*, 267–276.
Roemmich, D., and W. B. Owens (2000), The Argo Project: Global ocean observations for understanding and prediction of climate variability, *Oceanography*, *13*(2), 45–50.
Schade, L. R., and K. A. Emanuel (1999), The ocean's effect on the intensity of tropical cyclones: Results from a simple coupled atmosphere-ocean model, *J. Atmos. Sci.*, *56*, 642–651.
Scoccimarro, E., S. Gualdi, A. Bellucci, A. Sanna, P. G. Fogli, E. Manzini, M. Vichi, P. Oddo, and A. Navarra (2011), Effects of tropical cyclones on ocean heat transport in a high resolution coupled general circulation model, *J. Clim.*, *24*(16), 4368–4384, doi:10.1175/2011JCLI4104.1.
Shay, L. K., P. G. Black, A. J. Mariano, J. D. Hawkins, and R. L. Elsberry (1992), Upper ocean response to hurricane Gibert, *J. Geophys. Res.*, *97*, 20,227–20,248.

Sprintall, J., and M. Tomczak (1992), Evidence of the barrier layer in the surface layer of the tropics, *J. Geophys. Res.*, *97*, 7305–7316.
Sriver, R. L., and M. Huber (2007), Observational evidence for an ocean heat pump induced by tropical cyclones, *Nature*, *447*, 577–580, doi:10.1038/nature05785.
Wang, G., Z. Ling, and C. Wang (2009), Influence of tropical cyclones on seasonal ocean circulation in the South China Sea, *J. Geophys. Res.*, *114*, C10022, doi:10.1029/2009JC005302.
Wang, W., and R. X. Huang (2004), Wind energy input to the surface waves, *J. Phys. Oceanogr.*, *34*, 1276–1280.
Wang, X. D., G. J. Han, Y. Q. Qi, and W. Li (2011), Impact of barrier layer on typhoon-induced sea surface cooling, *Dyn. Atmos. Oceans*, *52*, 367–385, doi:10.1016/j.dynatmoce.2011.05.002.
Wang, X. D., C. Z. Wang, G. J. Han, W. Li, and X. R. Wu (2014), Effects of tropical cyclones on large-scale circulation and ocean heat transport in the South China Sea, *Clim. Dyn.*, doi:10.1007/S00382-014-2109-5, in press.
Wong, A. P. S., G. C. Johnson, and W. B. Owens (2003), Delayed-mode calibration of autonomous CTD profiling float salinity data by θ-S climatology, *J. Atmos. Oceanic Technol.*, *20*, 308–318.
Wu, Q. Y., and D. Chen (2012), Typhoon-induced variability of the oceanic surface mixed layer observed by Argo Floats in the Western North Pacific Ocean, *Atmos. Ocean*, *50*, suppl. 1, 4–14, doi:10.1080/07055900.2012.712913.
Yu, L., and R. A. Weller (2007), Objectively analyzed air-sea heat fluxes (OAFlux) for the global oceans, *Bull. Am. Meteorol. Soc.*, *88*, 527–539.
Yu, L., X. Jin, and R. A. Weller (2008), Multidecade global flux datasets from the objectively analyzed air-sea fluxes (OAFlux) project: Latent and sensible heat fluxes, ocean evaporation, and related surface meteorological variables, *OAFlux Proj. Tech. Rep. OA-2008-01*, 64 pp., Woods Hole Oceanogr. Inst., Woods Hole, Mass.
Zheng, Z. W., C. R. Ho, and N. J. Kuo (2008), Importance of pre-existing oceanic conditions to upper ocean response induced by Super Typhoon Hai-Tang, *Geophys. Res. Lett.*, *35*, L20603, doi:10.1029/2008GL035524.